

1 **Title Goes Here**

2 **Elio Campitelli · Leandro B. Díaz ·**
3 **Carolina Vera ·**

4
5 Received: date / Accepted: date

6 **Abstract** abstract
7

8 **Keywords** ·

The research was supported by UBACyT20020170100428BA and the CLIMAX Project funded by Belmont Forum/ANR-15-JCL/-0002-01. Elio Campitelli was supported by a PhD grant from CONICET, Argentina.

Elio Campitelli

Universidad de Buenos Aires, Facultad de Ciencias Exactas y Naturales, Departamento de Ciencias de la Atmósfera y los Océanos, Buenos Aires, Argentina CONICET – Universidad de Buenos Aires, Centro de Investigaciones del Mar y la Atmósfera (CIMA), Buenos Aires, Argentina CNRS – IRD – CONICET – UBA, Instituto Franco-Argentino para el Estudio del Clima y sus Impactos (UMI 3351 IFAECI), Buenos Aires, Argentina
E-mail: elio.campitelli@cima.fcen.uba.ar

Leandro B. Díaz

Universidad de Buenos Aires, Facultad de Ciencias Exactas y Naturales, Departamento de Ciencias de la Atmósfera y los Océanos, Buenos Aires, Argentina CONICET – Universidad de Buenos Aires, Centro de Investigaciones del Mar y la Atmósfera (CIMA), Buenos Aires, Argentina CNRS – IRD – CONICET – UBA, Instituto Franco-Argentino para el Estudio del Clima y sus Impactos (UMI 3351 IFAECI), Buenos Aires, Argentina

Carolina Vera

Universidad de Buenos Aires, Facultad de Ciencias Exactas y Naturales, Departamento de Ciencias de la Atmósfera y los Océanos, Buenos Aires, Argentina CONICET – Universidad de Buenos Aires, Centro de Investigaciones del Mar y la Atmósfera (CIMA), Buenos Aires, Argentina CNRS – IRD – CONICET – UBA, Instituto Franco-Argentino para el Estudio del Clima y sus Impactos (UMI 3351 IFAECI), Buenos Aires, Argentina

1 Introduction

introduction

2 Methods

methods

2.1 Data

data

We used monthly geopotential height, air temperature, ozone mixing ratio, and Total Ozone Column (TOC) at 2.5° longitude by 2.5° latitude of horizontal resolution and 37 vertical isobaric levels from ERA5 (Hersbach et al, 2019) for the period 1979 to 2019. We restricted most of our analysis to the post-satellite era to avoid any confounding factors arising from the incorporation of satellite observations, but we also used the preliminary back extension of ERA5 from 1950 to 1978 (Bell et al, 2020) to look at long-term trends. We derived streamfunction at 200 hPa from ERA5 vorticity using the FORTRAN subroutine FISHPACK (Adams et al, 1999) and computed horizontal wave activity fluxes following Plumb (1985) (Equation 5.7). For precipitation data we used monthly data from the CPC Merged Analysis of Precipitation (Xie and Arkin, 1997).

We computed the amplitude and phase of the zonal wave 1 by averaging variables (temperature, geopotential height, ozone mixing ratio and Total Ozone Column) 70°S and 45°S for each Spring and computing the Fourier spectrum.

We computed the level-dependent Southern Annular Mode index as the leading EOF of year-round monthly geopotential height anomalies south of 20°S at each level for the whole period (Baldwin and Thompson, 2009). We further split the SAM into its zonally symmetric and zonally asymmetric components (S-SAM and A-SAM indices respectively). These are obtained by projecting the zonally asymmetric and zonally symmetric part of the SAM spatial pattern onto monthly geopotential height fields (Campitelli et al, 2021). Since the analysis here is only for the SON trimester, monthly values were averaged across trimesters.

We also calculated the Pacific South American patterns (PSA1 and PSA2) as the third and fourth leading EOF of seasonal mean 500 hPa geopotential height with all seasons together following Mo and Paegle (2001).

2.2 Complex Empirical Orthogonal Functions

complex-empirical-orthogonal-functions

In traditional EOF analysis zonal waves appear as pairs of EOFs, usually degenerate, that represent similar patterns but shifted in phase. For instance, Figure 1 shows the leading 4 EOFs of zonally anomalous September through October geopotential height at 50 hPa and 100 hPa. It is clear that at 50 hPa the first two EFS represent the same zonal wave 1 pattern and the last 2 represent the same zonal wave 3 pattern shifted by $1/4$ wavelength. Since these pairs of EOFs seem to represent the same phase-varying structure, it

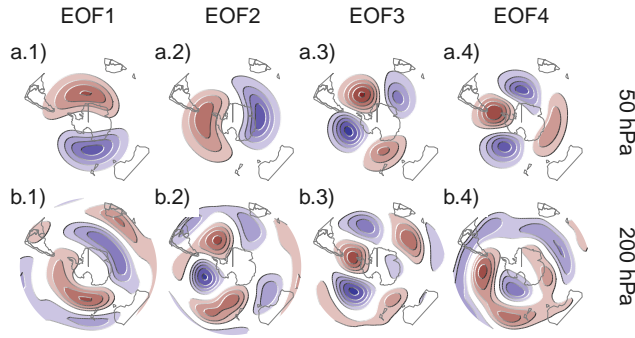


Fig. 1: Spatial patterns of the leading 4 EOFs of zonal anomalies of geopotential height at 50 hPa and 200 hPa for the SON trimester and the period 1979 – 2009 (arbitrary units). The numbers at the top-left of each panel are the zonal variance explained by each EOF.

Table 1: R^2 of the absolute magnitude of complex EOFs between 200 hPa and 50 hPa computing EOF separately for each level.

200 hPa	50 hPa		
	PC1	PC2	PC3
PC1	0.28	0.02	0.02
PC2	0.00	0.60	0.02
PC3	0.00	0.00	0.01

would be desirable to combine them into a single index with amplitude and phase.

Complex Empirical Orthogonal Functions (cEOF) is a useful method to characterise these waves (Horel, 1984). This method involves augmenting the original fields with the Hilbert transform of the data and then computing the Singular Value Decomposition of it. In this work, instead of applying the Hilbert transform to the time series at each point, we apply it to each latitude circle at each moment in time. Since the latitude circle is a periodic domain, this procedure does not suffer from edge effects.

The result of the cEOF is a set of complex spatial patterns and complex time series. The real and imaginary part of each spatial pattern represent two phases wave-like spatial pattern that are in quadrature. The magnitude and argument of each complex time series represent the amplitude and phase of each zonal wave.

Another characteristic seen in Figure 1 is that EOF1 at 200 hPa is very similar to EOF1 at 50 hPa. The zonal wave 3 structure in EOF2 and EOF3 at 200 hPa are also very similar to the one in EOF3 and EOF4 at 50 hPa. Furthermore, Table 1 shows the coefficient of determination between time series of the amplitude of each complex EOF across levels. There's a high degree of correlation between the respective EOF1 and EOF2 at each level.

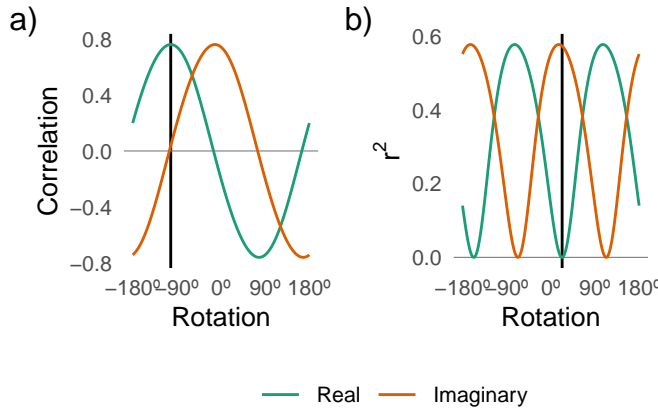


Fig. 2: a) Correlation of the Real and Imaginary EOF1 with wave 1 amplitude of Total Ozone Column averaged between 70°S and 45°S and b) R^2 between the Real and Imaginary EOF2 and the ONI index for different values of rotation. The vertical line marks the selected rotation, which maximises the correlation.

Both the spatial similarities and temporal correlations suggest some level of joint variability between levels.

Both observations motivate the decision of performing complex EOF jointly between levels. The computation of the EOFs was carried out using data from both levels at the same time, therefore, each complex EOF has a spatial part that depends on longitude, latitude and level, and a temporal part that depends only on time.

The phase of principal components is defined up to an additive constant. For real principal components, this constant can be either 0 or π , corresponding to a change in sign. For complex principal components, it can be any number between 0 and 2π (Horel, 1984). Since any choice is arbitrary and equally valid, we chose the phase of each EOF so that the real and imaginary parts are aligned with meaningful phases in our analysis. This was done after some exploratory analysis.

For the first complex principal component, the phase was chosen so that the time series corresponding to the real part has the maximum correlation with the zonal wave 1 of Total Ozone Column between 70°S and 45°S. This also nearly minimises the correlation with the imaginary part (Figure 2a).

For the second complex principal component, the phase was chosen so that the coefficient of determination between the Oceanic Niño Index (Bamston et al, 1997) and the real part was minimised, which also nearly maximises the correlation with the imaginary part (Figure 2b). It's important to reassure the reader that this procedure does not create a spurious correlation, it only takes whatever relationship that already exist and aligns it with a specific phase. If the relationship is very weak, the rotation cannot generate a strong relationship.

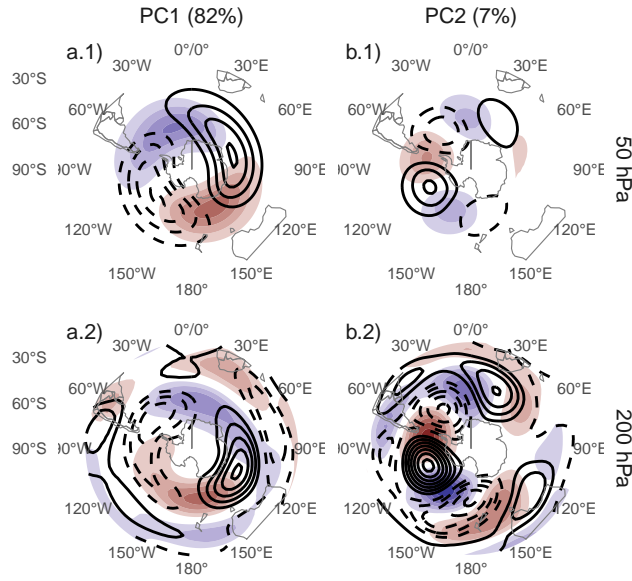


fig:ceofs-1
 Fig. 3: Spatial patterns of the leading 2 complex EOFs of zonal anomalies of geopotential height in 50 hPa and 200 hPa for the SON trimester and the period 1979 – 2009. Real part in shading, imaginary part in contours

2.3 Computation procedures

computation-procedures

We performed all analysis in this paper using the R programming language (R Core Team, 2020), using the data.table package (Dowle and Srinivasan, 2020) and the metR package (Campitelli, 2020). All graphics are made using ggplot2 (Wickham, 2009). We downloaded data from reanalysis using the ecmwfr package (Hufkens, 2020) and indices of the ENSO with the rsoi package (Albers and Campitelli, 2020). The paper was rendered using knitr and rmarkdown (Xie, 2015; Allaire et al, 2019).

3 Results

results

3.1 Description of EOFs

description-of-eofs

Figures 3 and 4 show, respectively, the spatial and temporal parts of the first two leading complex EOFs of zonal anomalies of geopotential height at 50 hPa and 200 hPa. In the spatial patterns in Figure 3, the real (in shading) and the imaginary parts (in contour) are in quadrature by construction, so that each EOF describe a single wave-like pattern whose amplitude and position (i.e. phase) is controlled by the magnitude and phase of the complex temporal EOF.

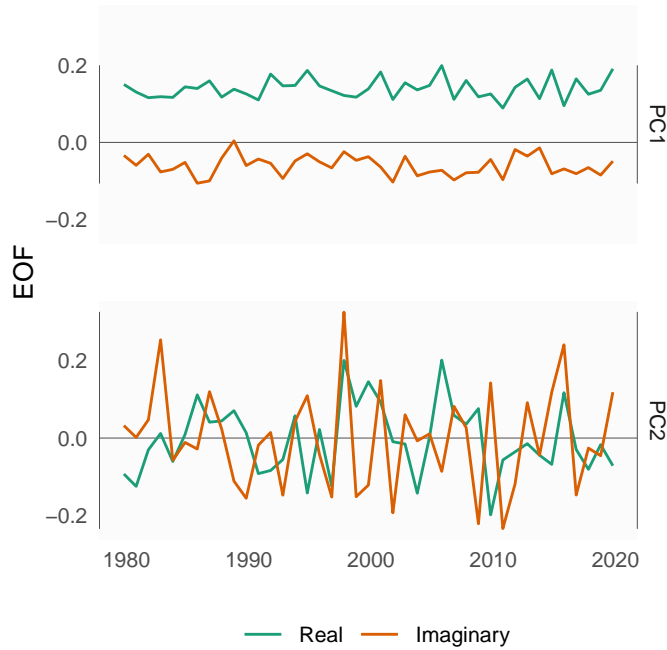


fig:ceofs-2
 Fig. 4: Time series of the leading 2 complex EOFs of zonal anomalies of geopotential height in 50 hPa and 200 hPa for the SON trimester and the period 1979 – 2009.

The wave patterns described by these complex EOFs match the patterns seen in the traditional EOFs of Figure 1: The first is a wave 1, while the second is a wave 3. Note that in Figure 4, both parts of the EOF1 have non zero mean. This is due to the fact that the geopotential fields that enter into the algorithm are anomalies with respect to the zonal mean, not the time mean. The variability associated with the first EOF includes variability that projects onto the mean zonally anomalous field.

Figure 5 shows time series of the two complex EOFs extended beyond the satellite era using the preliminary ERA5 back extension going back to 1950. There is an upward trend in the real part of EOF1 (Figure 5a.1, p-value < 0.001) and no significant trend in any of the complex parts of EOF2. The positive trend in the Real EOF1 translates into a positive trend in EOF1 magnitude, but not in phase (not shown).

3.2 Regressions

regressions

The spatial patterns shown in Figure 3 are “pure” EOF patterns. But as they are derived by removing the zonally symmetric circulation, they might not include all the variability that is actually associated with the EOF time

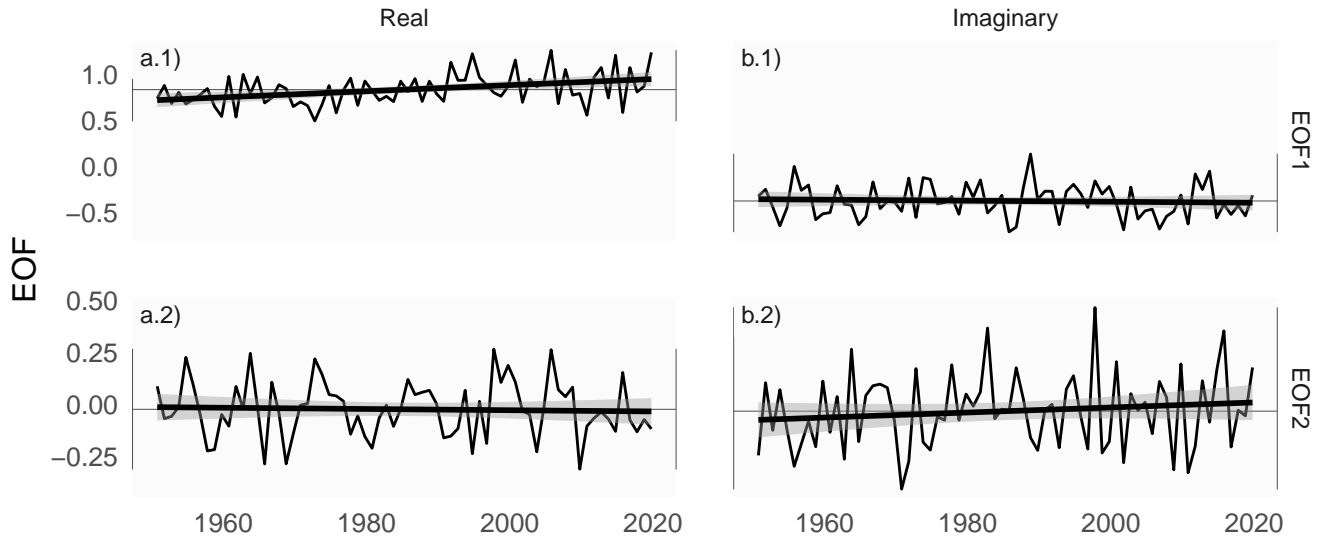


Fig. 5: Time series extended using ERA5 back extended preliminary edition (period 1950 – 1978) and ERA5 (period 1979 – 2019). Each series is computed by projecting monthly geopotential height zonal anomalies standardised by level south of 20°S onto the corresponding spatial pattern and scaled to zero mean and unit standard deviation.

fig:extended-series

series. They are also idealised in that they are forced by construction, to be Hilber transforms of each other. To get a more realistic view of the real-world variability described by these EOFs, we computed regression patterns of each EOF with the complete geopotential fields.

Figure 6 shows regression patterns of EOF1 and geopotential height. At 50 hPa (Figure 6 row a), both the Real and Imaginary EOF1 are associated with planetary wave 1 patterns, that are 90° off phase. Their phases coincide with the ones shown in Figure 3a.1, with the positive centre of the Real EOF1 located towards the dateline, and the one of the Imaginary EOF1 located over Eastern Antarctica. However, the Real EOF1 pattern is substantially altered by the zonally symmetric circulation. Instead of a clear wave 1 pattern, the regression pattern can be better describes as a monopole with its centre displaced from the South Pole.

Similarly affected are the regression patterns at 200 hPa (Figure 6 row b). It is only possible to distinguish some of the wave 1 pattern in relation with the Real EOF1 (Figure 6b.1). The Imaginary EOF1 shows a much more zonally symmetrical pattern resembling a negative Southern Annular Mode.

With the exception of the Imaginary EFO1, it's clear that these patterns are very different than the idealised versions shown in Figure 3, particularly at 200 hPa. Moreover, only in the stratosphere these patterns actually show a distinguishable wave 1 pattern shifted in phase by 90°. This should not be utterly surprising, since the spatial patterns of the *naïve* EOFs only show this

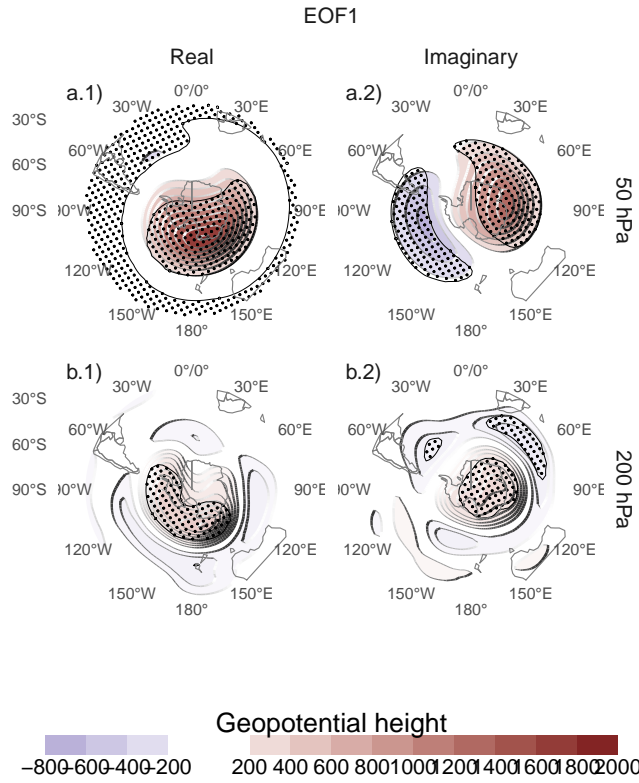


Fig. 6: Regression coefficients of the real and imaginary part of the first complex EOF on SON geopotential height for the 1979 – 2019 period. These coefficients come from multiple linear regression involving the real and imaginary part of both EFO2.

feature at 50 hPa, suggesting that using the complex EOF method is “forcing” a wave structure where there is none.

Therefore, the magnitude and phase of the EOF1 are associated with the magnitude and phase of a zonal wave only in the stratosphere. While in the troposphere they are associated with slightly off-centre monopoles.

Figure 7 shows the regression pattern of geopotential height and the EOF2. Unlike in the case of EOF1, in this case the regression patterns represent relatively well the *idealised* patterns from Figure 3. Although there are some differences (particularly in 50 hPa), the wave trains identified before are well characterised and patterns associated with the Real EOF2 are 90° out of phase with those associated with the Imaginary EOF2. Zonal wave 3 dominates all fields, but only in the western hemisphere.

EOF2 then represents a equivalent barotropic wave train that is very similar to the the Pacific South American Patterns (Mo and Paegle, 2001). Comparing the location of the positive anomaly near 90°W in column b of Figure 7

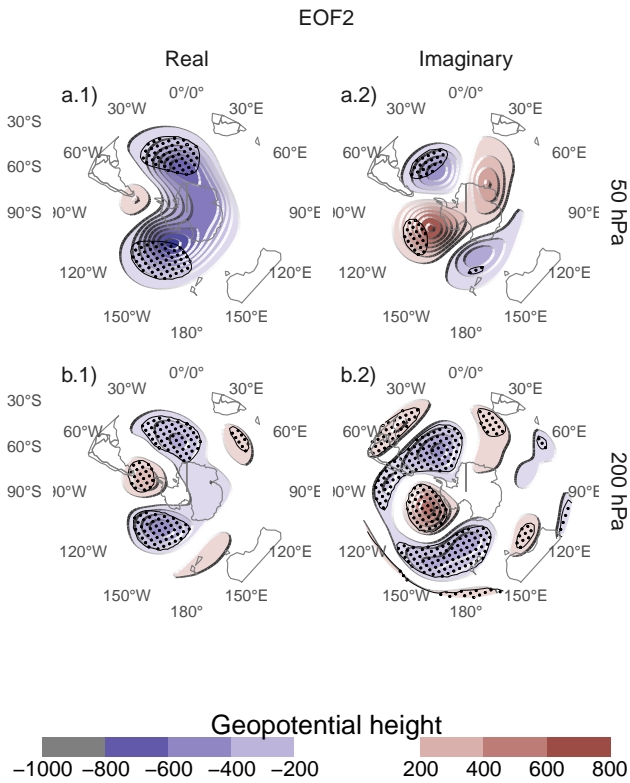


fig:eof2-regr-gh
Fig. 7: Same as Figure 6 but for the second EOF.

with Figure 1 a and b from Mo and Paegle (2001), the Real EOF2 can roughly be identified with the PSA2, while the Imaginary EOF2 resembles PSA1. This separation is not completely meaningful in this case, since by treating this pattern as a single wave train any one pair of orthogonal waves can characterise this variability.

3.3 Relationship with other variables

relationship-with-other-variables

3.3.1 Ozone

ozone

Figure 8 shows regression patterns of EOF1 with air temperature. In both levels, the distribution of temperature anomalies mirror the geopotential height anomalies in 50 hPa. To understand the vertical distribution of these anomalies, Figure 9) shows the regression pattern of EOF1 with zonal anomalies of air temperature and zonal anomalies of ozone mixing ratio averaged between 80°S and 35°S. Temperature zonal anomalies associated with EOF1 show a clear wave 1 pattern throughout the atmosphere above 200 hPa with a change

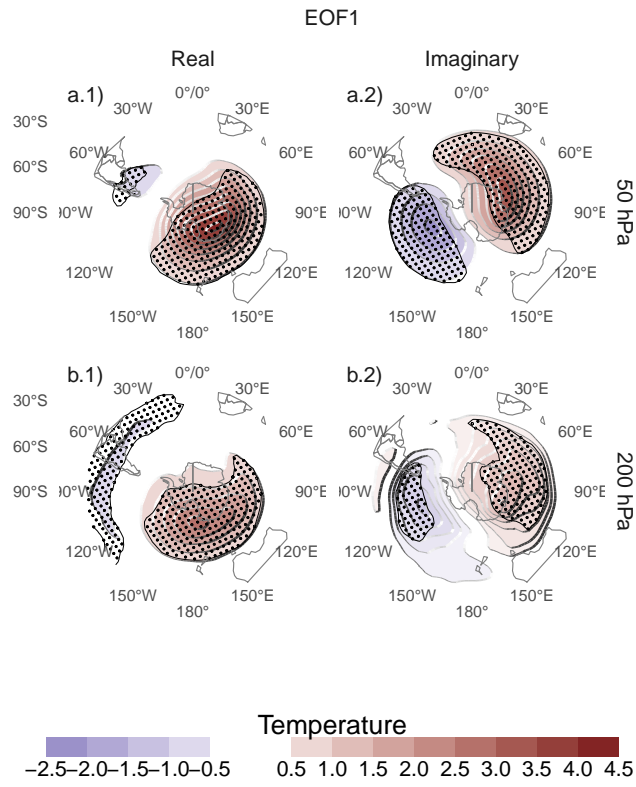


Fig. 8: Same as Figure 6 but for air temperature.

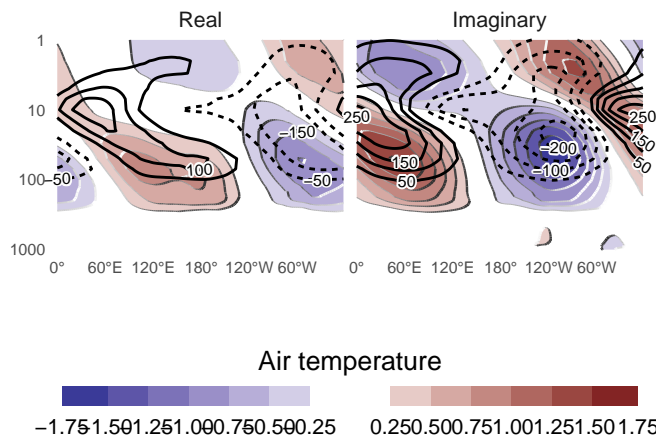


Fig. 9: Regression of EOF1 with zonal anomalies of mean air temperature (shaded) and ozone mixing ratio (contours, negative contours with dashed lines, labels in parts per billion by mass) averaged between 80°S and 25°S for the period 1979 – 2019.

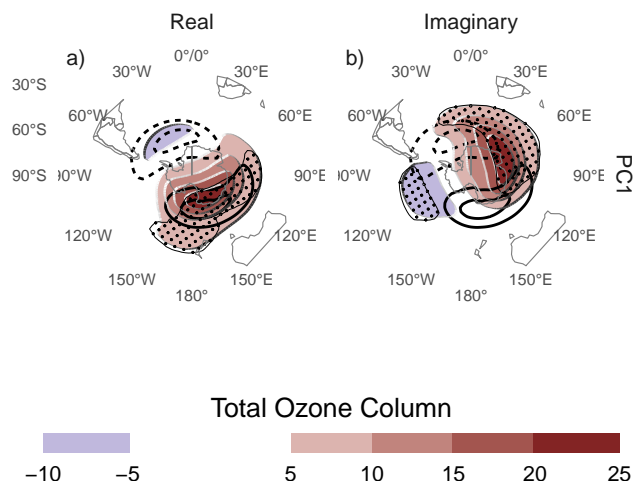


Fig. 10: Regression coefficients of the real and imaginary part of the first complex EOF on SON mean Total Ozone Column. On contours, the mean zonal anomaly of Total Ozone Column (negative contours in dashed lines). For the 1979 – 2019 period.

in sign above 10 hPa. Following hydrostatic balance, this is the level in which the geopotential anomaly have maximum amplitude (not shown).

The maximum ozone anomalies are co-located with the minimum temperature anomalies above 10 hPa and with the maximum temperature anomalies below 10 hPa; that is, the ozone zonal wave 1 is anticorrelated with the temperature zonal wave 1 in the upper stratosphere, and directly correlated in the upper stratosphere. This change in phase is observed in ozone anomalies forced by planetary waves that reach the stratosphere. In the photochemically-dominated upper stratosphere, cold temperatures inhibit the destruction of ozone, and the advectively-dominated lower stratosphere, ozone anomalies are 90° out of phase with horizontal and vertical transport, which is 90° out of phase with temperature anomalies (Hartmann and Garcia, 1979; Wirth, 1993; Smith, 1995).

Figure 10 shows regression maps of EOF1 with fields of Total Ozone Column (TOC). It shows zonal wave 1 patterns in TOC associated with both phases of EOF1. Climatologically, the springtime Ozone minimum is located off the South Pole and towards the Weddell Sea (Wirth, 1993). Thus, the Real EOF1 regression pattern (Figure 10a) coincides with the climatological position of the ozone hole while the one for the Imaginary EOF1 is shifted by 90°.

Indeed, Figure 11 shows the relationship between amplitude and phase of the planetary wave 1 in Total Ozone Column between 70°S and 45°S and amplitude and phase of the EOF1. The correlation between the zonal wave 1 of ozone and EOF1 (computed as the mean cosine of the difference in phase) is

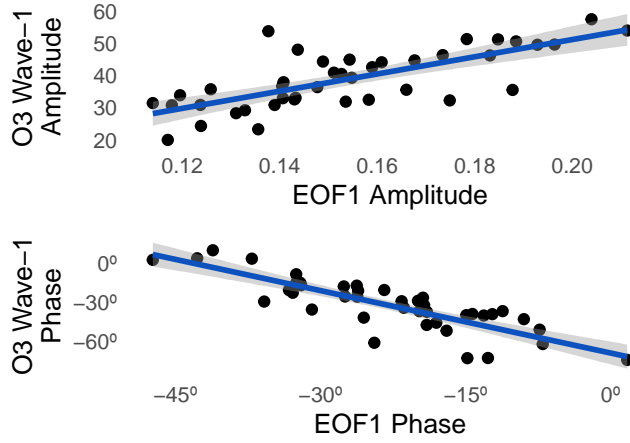


Fig. 11: Relationship between EOF1 amplitude and phase with amplitude and phase of the zonal wave 1 in Total Ozone Column averaged between 70°S and 45°S for the period 1979 – 2019.

0.86 (CI: 0.76 – 0.93). As expected from the location of anomalies in Figure 11, the Real EOF1 drives the relationship with amplitude and the Imaginary EOF1 drives the relationship with phase (not shown).

3.3.2 PSA

We will show that the EOF2 offers an alternative way of representing the PSA which has several advantages over using the second and third principal components .

Figure 12 shows the relationship between the two PSA indices and the Real and Imaginary phase of EOF2. As anticipated by Figure 7, there is a strong correlation between PSA1 and Imaginary EOF2 (Figure 12b.1), and between PSA2 and Real EOF2 (Figure 12a.2). Conversely, there is no relationship between PSA1 and Real EOF2, and between PSA2 and Imaginary EOF2 (Figure 12 panels a.1 and b.2). So not only this EOF2 represents well both the spatial structure and temporal evolution of the PSA modes, but it's also possible to make a rather clean association between its two phases and the two PSA modes.

This particular rotation of EOF2 is the one which maximises the relationship between ENSO and Imaginary EOF2. It is also the same that maximises this clean association between EOF2 parts and PSA modes. The reason that the “naive” principal component analysis arrives naturally to this optimal separation is that the imaginary phase is the most common phase (Figure 13), so it naturally appears first when performing a Principal Component Analysis.

By aligning the imaginary phase with the direction with maximum relationship with ENSO, we also aligned it with the phase of maximum occurrence. This is analogous to the method in Irving and Simmonds (2016), who used

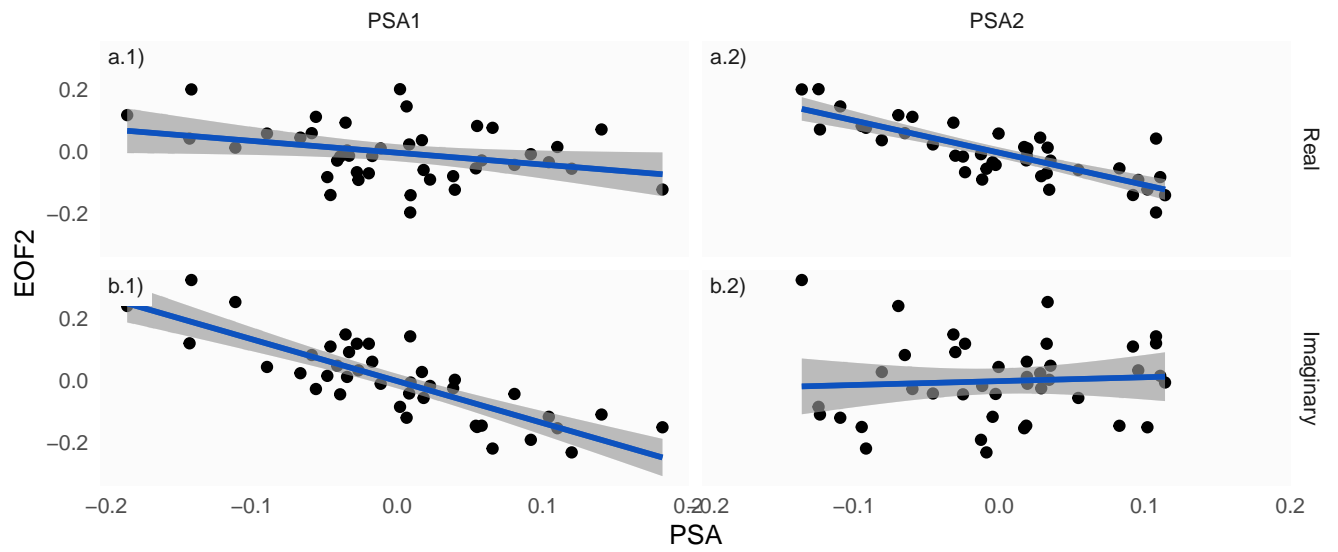


Fig. 12: Relationship between the Real and Imaginary parts of EOF2 and the PSA1 and PSA2 modes computed as the second and third EOFs of seasonal geopotential height anomalies (Mo and Paegle, 2001). For the period 1979 – 2019.

fig:psa-eof2

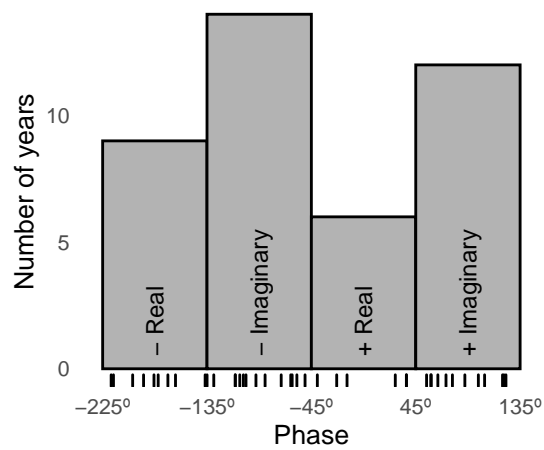


Fig. 13: Histogram showing phase distribution of EOF2 for the period 1979 – 2019.

fig:phase-histogram

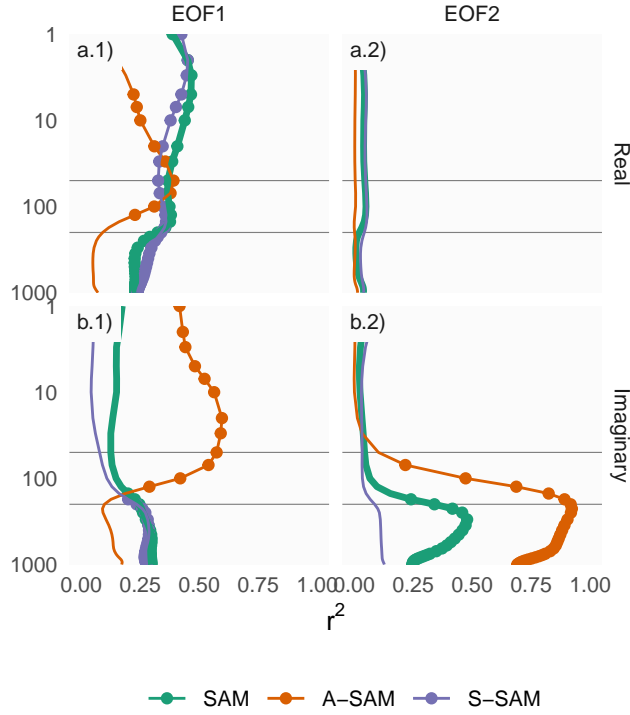


fig:sam-eof-vertical
 Fig. 14: Coefficient of determination between the real and imaginary part of each EOF and the SAM, Asymmetric SAM (A-SAM) and Symmetric SAM (S-SAM) indices computed at each level according to Campitelli et al (2021). Points mark estimates with p-value < 0.01 corrected for False Detection Rate (Benjamini and Hochberg, 1995).

reprojection and Fourier filtering to detect “PSA-like” variability and defined as the proper PSA using the peaks of the phase distribution (Compare our Figure @ref:(phase-histogram) with their Figure 6).

The advantage of our method is that it is much simpler to implement, it provides magnitude and phase naturally, and it facilitates the description of this mode as a propagating wave instead of as standing oscillation.

3.3.3 SAM

Figure 14 shows the coefficient of determination between the EOFs and three SAM indices.

Both EOFs bear some modest relationship with the SAM index (thick green line in Figure 14), although not statistically significant at every level. The split between A-SAM and S-SAM gives more insight into the nature of the relationship. The relationship between the SAM and the imaginary EOF1

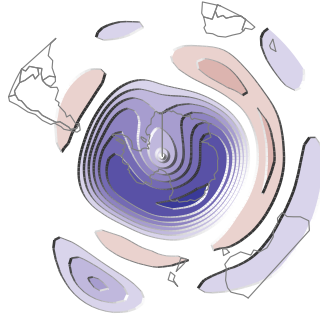


Fig. 15: ^{fig:eof-filtered} Spatial pattern of the leading EOF of 200 hPa geopotential height with the variability of EOF2 filtered out South of 20°. Arbitrary units.

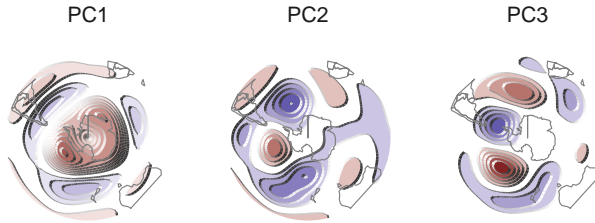


Fig. 16: ^{fig:fake-eof} EOFs of a synthetic data set of 41 time steps of geopotential height fields as the sum of the fields predicted by the EOF2 plus perfectly zonally symmetric SAM-like anomalies with random amplitude.

(Figure 14.b1) is mediated by S-SAM in the troposphere, but by the A-SAM in the stratosphere.

The Imaginary EOF2 is related with the SAM through the A-SAM in the troposphere, with up to -96% of shared variance, reached at 225 hPa (Figure 14.b2).

As a further illustration, Figure 15 shows the spatial pattern of the leading EOF of 200 hPa geopotential height when the variability associated with EOF2 is removed. The resulting pattern is an nearly zonally symmetrical annular mode. This mode is highly correlated with SAM (0.75 (CI: 0.58 – 0.86)), but only with the symmetrical part (0.88 (CI: 0.79 – 0.94)). Note that the usual definition of the PSA modes as the second and third EOFs creates modes orthogonal to the SAM (defined as the first EOF) and thus impedes this kind of filtering.

This suggests that the asymmetric part of the SAM might be statistical contamination from one phase of the PSA. Figure 16 serves as an illustration of this kind of statistical mixing of independent modes. It shows the leading (and only) EOFs of a synthetic dataset of 41 years created by adding a perfectly zonally symmetrical SAM-like pattern with random amplitudes taken from the real SAM, and geopotential height anomalies predicted by EFO2. Even though by construction this dataset has a perfectly symmetric SAM, the EOF

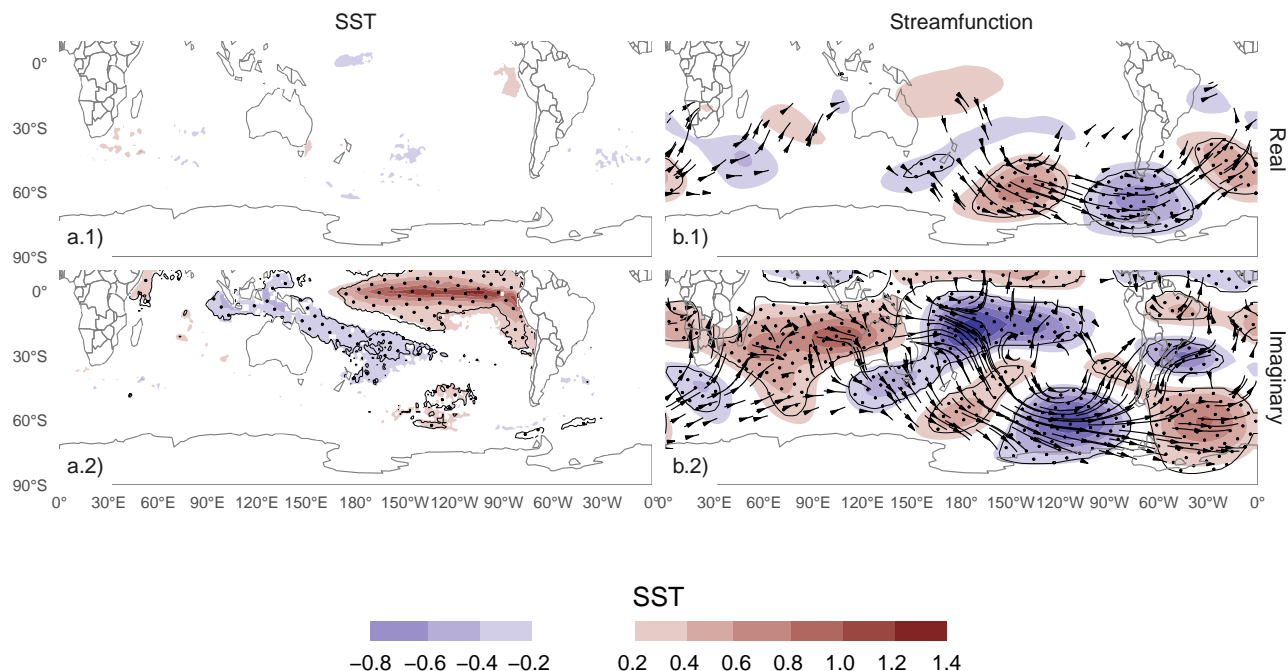


Fig. 17: Regression maps of EOF2 with SST (column a) and streamfunction zonal anomalies with their corresponding activity wave flux (column b). Areas marked with dots have p-values smaller than 0.05 adjusted for FDR. fig:sst-psi-2

decomposition mixes this mode with parts of the the zonally asymmetric EOF2 pattern, resulting in a pattern eerily similar to the real SAM pattern.

This demonstrates that the zonal asymmetries of the SAM could very well be mostly a statistical artifact. Since many surface impacts are mediated by the asymmetric component, as well as the relationship between SAM and ENSO (Campitelli et al, 2021), this potential issue could affect the interpretability of many results involving the SAM. Studies on the relationship between the SAM and the PSA pattern would be particularly difficult to interpret.

3.4 Tropical sources

tropical-sources

Figure 17 shows regression maps between EOF2 and Sea Surface Temperatures (SST) Streamfunction at 200 hPa. The Imaginary EOF2 is associated with strong positive SST anomalies on the Central Pacific and negative anomalies on an area across the North of Australia and New Zealand, the South Pacific Convergence Zone (SPCZ) (Figure 17.a2). This pattern is almost canonically positive ENSO and indeed, the correlation between the Imaginary EOF2 and the Oceanic Niño Index ((Bamston et al, 1997)) is very high 0.76 (CI: 0.59 – 0.86). Streamfunction anomalies show a coherent picture. The Imaginary

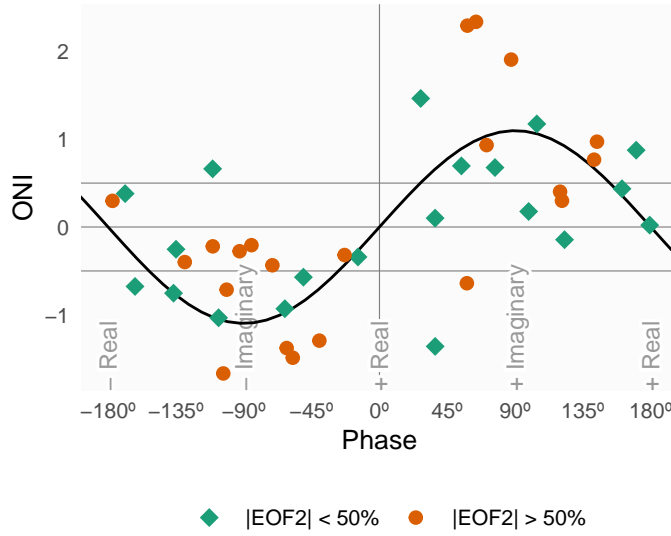


fig:enso-phase
 Fig. 18: Relationship between ENSO and phase of EOF2 for the period 1979 – 2019. Colours denote years with magnitude of EOF2 greater or smaller than the 50th percentile. Black line is the fit $ONI \sim \cos(\text{phase}) + \sin(\text{phase})$ computed by OLS weighted by the magnitude of EOF2.

EOF2 is associated with strong wave-like streamfunction anomalies emanating from the tropics (Figure 17.b2). This is consistent with what we know of the effect of ENSO on the extratropics: SST anomalies initiate anomalous convection that excites Rossby waves that propagate meridionally towards higher latitudes.

Since the Real EOF2 represents just a different phase of the same wave train, one would expect that it would show a similar forcing pattern to the Imaginary EOF with a slight translation of its location. However, Figure 17.a1 and b1 show that the Real EOF2 is not associated either with any significant SST nor streamfunction anomalies in the tropics. The correlation between the Real EOF2 and ENSO is also not significant ($r^2 = 0.01$). This lack of tropical signal suggests a radically different nature of the different phases of the EOF2 wave train.

To better explore the relationship between tropical forcing and phase of the EOF2, Figure 18 plots the ONI index and the phase of the EOF2 for each year between 1979 and 2019, highlighting years in which the magnitude of EOF2 was higher than 50% of the years. In years with positive ENSO, the phase of the EOF2 is always around $+90^\circ$ (corresponding with positive imaginary part) and vice versa. In years with near neutral ENSO, the phase of the EOF2 is much more variable. The black line in Figure 18 tries to quantify this relationship. Is the equation $ONI = 1.1 \sin(\text{phase})$, whose coefficient we fitted by weighted least squares using the magnitude of the EOF2 as weight. The r^2 corresponding to the fit is 0.56, with p-value < 0.001 .

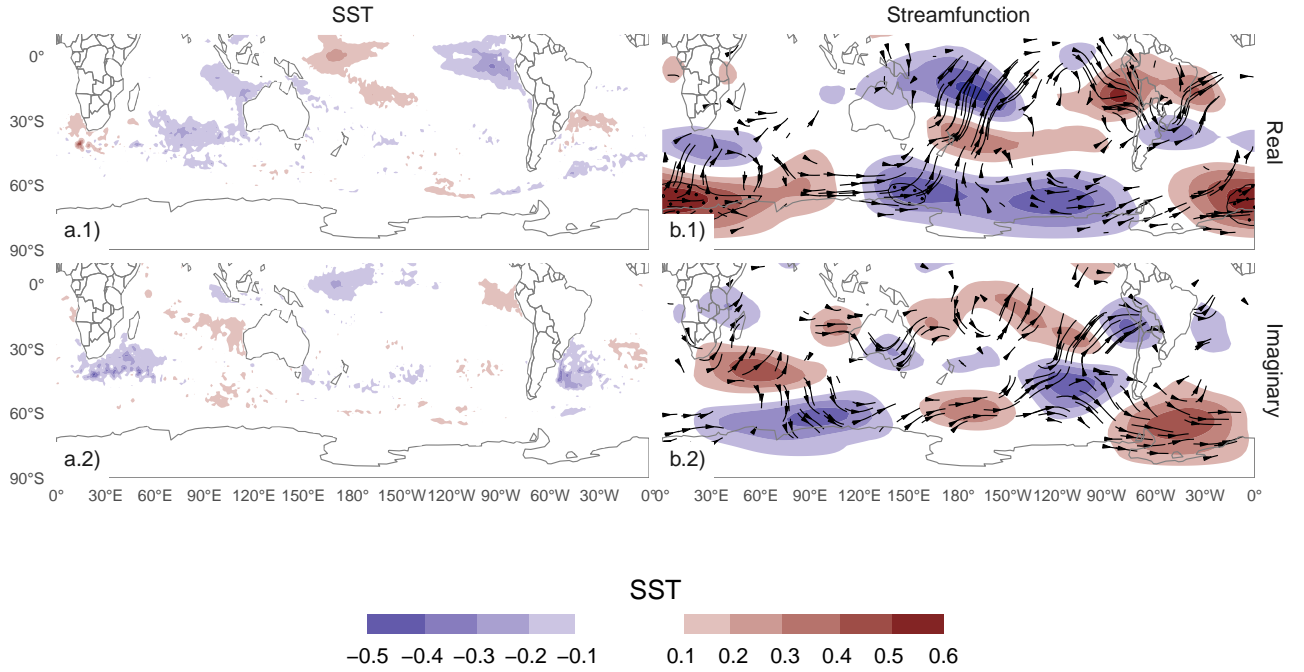


Fig. 19: Same as Figure 17 but for EOF1.

fig:sst-psi-1

Figure 18 suggest that strong EOF2 years tend to coincide with strong ENSO years. The correlation between the absolute magnitude of the ONI and the magnitude of the EOF2 is 0.44 (CI: 0.16 – 0.66). This relationship, however, appears to be driven only by the three years with strongest ENSO events in the period (2015, 1997, and 1982) which also coincide with the three years with strongest EOF2 magnitude. If those years are removed, the correlation becomes non-significant (0.044 (CI: -0.28 – 0.36)). Furthermore, even when using all the datapoints, the Spearman correlation –which is robust to outliers– is also non-significant (0.2, p-value = 0.2). Therefore, the relationship between the magnitude of the EOF2 train wave and ENSO remains uncertain.

All this suggests that the wave train represented by EOF2 can be both forced by tropical SSTs and also a part of the internal variability of the extra-tropical atmosphere. When internally forced, the wave train has little phase preference. When excited by tropical SST anomalies, it tends to remain locked to the imaginary phase, with the sign of the geopotential anomalies depending on the sign of the tropical SSTs anomalies. This explains the relative overabundance of years with EOF2 near positive and negative imaginary phase in Figure 13.

Figure 19 shows SST and streamfunction regression maps for EOF1. There is no significant pattern of SST anomalies associated with either the Real or Imaginary EOF1. Consistently, streamfunction anomalies don't show any

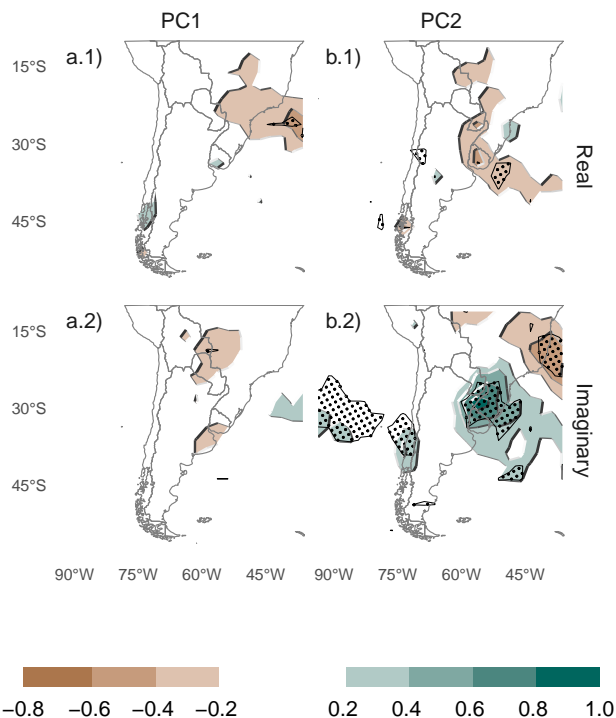


fig:pp-america
 Fig. 20: Regression of SON mean precipitation anomalies in South America (mm per day, shaded) and (column a) EOF1 the (row 1) Imaginary and (column 1) Real phase. For the 1979 – 2018 period. Black contours with dots indicate areas with p-value smaller than 0.05 controlling for False Detection Rate.

tropical influence. On the contrary, the Real EOF1 is associated with wave activity fluxes that flow equatorward from the coast of Antarctica around 150°E along with wave activity fluxes that move between the positive and negative of Streamfunction anomalies along Antarctica.

3.5 Precipitation

precipitation
 Figure 20 shows regression maps of seasonal precipitation with each EOF in South America. EOF1 is associated with slight decreases in precipitation in Southern Brazil and Paraguay, although these are not statistically significant 20 column a. The strongest precipitation anomalies are the ones associated with the Imaginary EOF2. The positive anomalies on Southeaster South America (SESA) and Chile, and negative anomalies over Southern Brazil is a well known springtime precipitation signature of ENSO (Cai et al, 2020) and it's also virtually identical to the precipitation anomalies associated with the

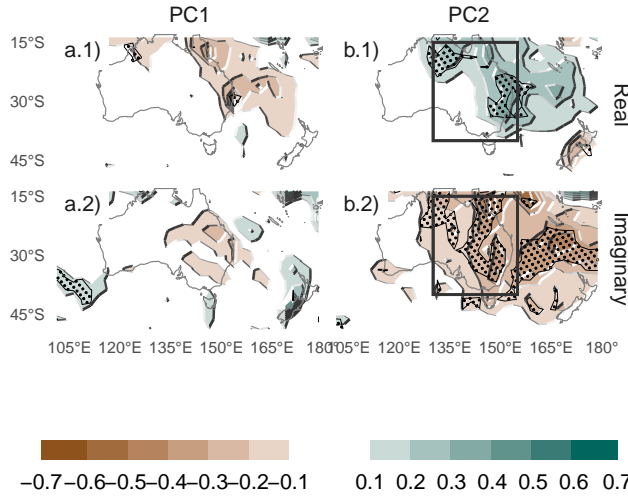


Fig. 21: Same as Figure 20 but for New Zealand and neighbouring islands.

Asymmetric SAM (Campitelli et al, 2021). This is not surprising considering the close relationship between the ONI, the Asymmetric SAM index and the Imaginary EOF2 shown previously, but further consolidates the identification of this mode with the PSA pattern. The Real EOF2, on the other hand, is associated with negative precipitation anomalies in a smaller area of SESA. The relationship between precipitation anomalies in SESA and the phase of EOF2 follows a curve similar to that of Figure 18 (not shown).

On the antipodes, precipitation anomalies in New Zealand and neighbouring islands associated with EOF1 are also weak and not statistically significant (Figure 21 column a) whereas EFO2 is associated with large and expansive anomalies. The Real EOF2 is associated with positive seasonal anomalies in Northern and Eastern Australia, and negative ones over New Zealand, while precipitation anomalies associated with Imaginary EOF2 are negative over all Eastern Australia. Again, these negative anomalies are similar to the spring-time precipitation anomalies observed in relation with the Asymmetric SAM (Campitelli et al, 2021).

To better understand the relationship between precipitation anomalies over Western Australia and the EOF2, Figure 22 plots precipitation anomalies averaged over Eastern Australia (box in Figure 21) as a function of EOF2 phase. The black line is the equation $\text{Precipitation} = -0.26 \sin(\text{phase}) + 0.22 \cos(\text{phase})$, whose coefficient we fitted by weighted least squares using the magnitude of the EFO2 as weight. The r^2 corresponding to the fit is 0.37, with p-value < 0.001 . There is a strong relationship between the phase of the EOF2 and precipitation anomalies in Eastern Australia, but Real and Imaginary phases we chose are not aligned with the direction that maximises this relationship. If one were to perform a more in-depth analysis of the relationship between this pattern and precipitation in this region, one would

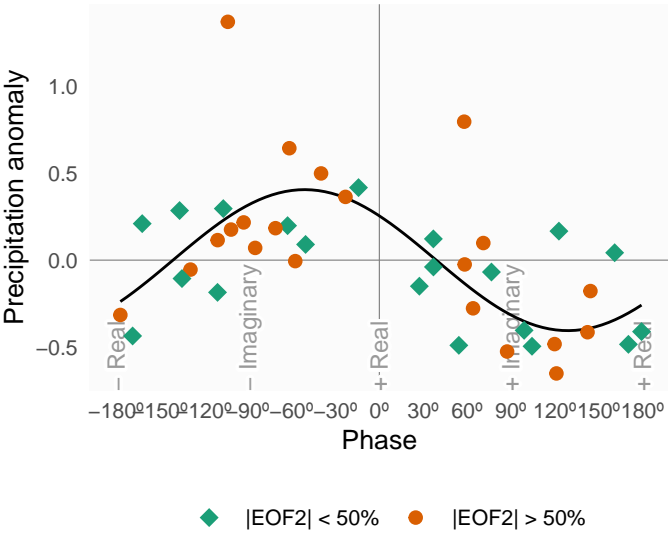


fig:australia-pp-phase
Fig. 22: Same as Figure 18 but for precipitation anomalies averaged between 130°E and 155°E and 40°S and 15°S (box shown in Figure 21 column b).

conceivably align one of the axis (either the Real or the Imaginary) to the one that maximises it.

4 Conclusions

Code availability

A version-controlled repository of the code used to create this analysis, including the code used to download the data can be found at <https://github.com/eliocamp/shceof>.

5 References

References

Adams JC, Swartztrauber PN, Sweet R (1999) FISHPACK, a package of Fortran subprograms for the solution of separable elliptic partial differential equations. <https://www2.cisl.ucar.edu/resources/legacy/fishpack>

Albers S, Campitelli E (2020) Rsoi: Import Various Northern and Southern Hemisphere Climate Indices

Allaire J, Horner J, Xie Y, Marti V, Porte N (2019) Markdown: Render Markdown with the c Library 'Sundown'

- Baldwin MP, Thompson DWJ (2009) A critical comparison of stratosphere–troposphere coupling indices. *Quarterly Journal of the Royal Meteorological Society* 135(644):1661–1672, DOI 10.1002/qj.479
- Bamston AG, Chelliah M, Goldenberg SB (1997) Documentation of a highly ENSO-related sst region in the equatorial pacific: Research note. *Atmosphere-Ocean* 35(3):367–383, DOI 10.1080/07055900.1997.9649597
- Bell B, Hersbach H, Berrisford P, Dahlgren P, Horányi A, Muñoz Sabater J, Nicolas J, Radu R, Schepers D, Simmons A, Soci C, Thépaut JN (2020) ERA5 monthly averaged data on pressure levels from 1950 to 1978 (preliminary version). Copernicus Climate Change Service (C3S) Climate Data Store (CDS) (Accessed on <19-02-2021>), <https://cds.climate.copernicus.eu/cdsapp#!/dataset/reanalysis-era5-pressure-levels-monthly-means-preliminary-back-extension?tab=overview>
- Benjamini Y, Hochberg Y (1995) Controlling the False Discovery Rate: A Practical and Powerful Approach to Multiple Testing. *Journal of the Royal Statistical Society: Series B (Methodological)* 57(1):289–300, DOI 10.1111/j.2517-6161.1995.tb02031.x
- Cai W, McPhaden MJ, Grimm AM, Rodrigues RR, Taschetto AS, Garreaud RD, Dewitte B, Poveda G, Ham YG, Santoso A, Ng B, Anderson W, Wang G, Geng T, Jo HS, Marengo JA, Alves LM, Osman M, Li S, Wu L, Karamperidou C, Takahashi K, Vera C (2020) Climate impacts of the El Niño–Southern Oscillation on South America. *Nature Reviews Earth & Environment* 1(4):215–231, DOI 10.1038/s43017-020-0040-3
- Campitelli E (2020) metR: Tools for Easier Analysis of Meteorological Fields
- Campitelli E, Diaz L, Vera C (2021) Assessment of zonally symmetric and asymmetric components of the Southern Annular Mode using a novel approach. *Climate Dynamics* (under review)
- Dowle M, Srinivasan A (2020) Data.table: Extension of 'data.frame'
- Hartmann DL, Garcia RR (1979) A Mechanistic Model of Ozone Transport by Planetary Waves in the Stratosphere. *Journal of the Atmospheric Sciences* 36(2):350–364, DOI 10.1175/1520-0469(1979)036<0350:AMMOOT>2.0.CO;2
- Hersbach H, Bell B, Berrisford P, Biavati G, Horányi A, Muñoz Sabater J, Nicolas J, Peubey C, Radu R, Rozum I, Schepers D, Simmons A, Soci C, Dee D, Thépaut JN (2019) ERA5 monthly averaged data on pressure levels from 1979 to present. Copernicus Climate Change Service (C3S) Climate Data Store (CDS) (Accessed on <08-03-2021>), DOI 10.24381/cds.6860a573
- Horel JD (1984) Complex Principal Component Analysis: Theory and Examples. *Journal of Applied Meteorology and Climatology* 23(12):1660–1673, DOI 10.1175/1520-0450(1984)023<1660:CPCATA>2.0.CO;2
- Hufkens K (2020) Ecmwfr: Programmatic interface to the two European Centre for Medium-Range Weather Forecasts API services
- Irving D, Simmonds I (2016) A New Method for Identifying the Pacific–South American Pattern and Its Influence on Regional Climate Variability. *Journal of Climate* 29(17):6109–6125, DOI 10.1175/JCLI-D-15-0843.1

- Mo KC, Paegle JN (2001) The Pacific–South American modes and their downstream effects. *International Journal of Climatology* 21(10):1211–1229, DOI 10.1002/joc.685
- Plumb RA (1985) On the Three-Dimensional Propagation of Stationary Waves. *J Atmos Sci* 42(3):217–229, DOI 10.1175/1520-0469(1985)042<0217:OTTDPO>2.0.CO;2
- R Core Team (2020) R: A Language and Environment for Statistical Computing. R Foundation for Statistical Computing, Vienna, Austria
- Smith AK (1995) Numerical simulation of global variations of temperature, ozone, and trace species in the stratosphere. *Journal of Geophysical Research: Atmospheres* 100(D1):1253–1269, DOI 10.1029/94JD02395
- Wickham H (2009) *Ggplot2: Elegant Graphics for Data Analysis*. Use R!, Springer-Verlag, New York, DOI 10.1007/978-0-387-98141-3
- Wirth V (1993) Quasi-stationary planetary waves in total ozone and their correlation with lower stratospheric temperature. *Journal of Geophysical Research: Atmospheres* 98(D5):8873–8882, DOI 10.1029/92JD02820
- Xie P, Arkin PA (1997) Global Precipitation: A 17-Year Monthly Analysis Based on Gauge Observations, Satellite Estimates, and Numerical Model Outputs. *Bull Amer Meteor Soc* 78(11):2539–2558, DOI 10.1175/1520-0477(1997)078<2539:GPAYMA>2.0.CO;2
- Xie Y (2015) *Dynamic Documents with R and Knitr*, 2nd edn. Chapman and Hall/CRC, Boca Raton, Florida